Research Article ISSN 2832-9384

Journal of Materials and Polymer Science

3D Thermal Study of Double Partition Brick Drying

Rzig Ramzi[1*], Minyar Mnakri[2] and Nidhal Ben Khedher[3]

[1]*Become: Technology, Science, AI & Automation Lab, 63 Street of Tolbiac, 75013 Paris, France*

[2]*Laboratory of Spectroscopic Characterization and Optical Materials LaSCOM, Sfax University, Sfax 3029, Tunisia*

[3]*Department of Mechanical Engineering, College of Engineering, Hail University, Hail 55476, Saudi Arabia*

***Correspondence author**
Rzig Ramzi
Become: Technology, Science,
AI & Automation Lab,
63 Street of Tolbiac,
75013 Paris, France

Submitted : 7 Mar 2023 ; Published : 3 Aug 2023

Citation : Rzig R., (2023). 3D Thermal Study of Double Partition Brick Drying. *J mate poly sci, 3*(3): 1-9.
DOI : https://doi.org/10.47485/2832-9384.1035

Abstract

In porous media, heat and mass transfer is a classical model of transport and it is one of the most energy-intensive industrial processes with a wide variety of applications. This present paper is developed in order to explain the coupled heat and mass transfer that arise during drying process. A free mesh generator Gmsh is used and a 3-D unstructured Control Volume Finite Element Method (CVFEM) is employed to simulate the transport phenomena with a convective drying. Several simulation results, that depict the transport phenomenon inside a porous brick are presented and analyzed. Indeed, thanks to this numerical model, we can observe the three-dimensional distribution of temperature, liquid saturation and pressure during double partition brick drying.

Keywords: CVFEM ; Double partition brick ; Drying ; Gmsh ; Porous media

Introduction

Simultaneous heat and mass transfer in porous media is one of the most important industrial processes and it is central to many applications involving industrial devices (heat transport, chemical engineering, heat exchangers, etc.). Also, the theoretical and experimental study of the heat and mass transfer in porous media has been the target of a lot of important research work. Most of the time, the cost and the time depicts a problem for experimental studies. However, the numerical modelling is widely used to analyze the coupled heat and mass transfer. Based on the theory of Luikov [1] and Whitaker [2], a mathematical system for transfer in porous media has been established with dynamic variables (temperature, gaseous pressure and liquid saturation).

The method of solution for the own problem is based on the control volume finite element approach which has been shown to be particularly well suited for a fast and efficient implementation of the linearization technique. Moreover, the finite difference solution has been widely used in the simulation of heat and mass transfer in porous media [3, 4]. Consequently, the Control Volume Finite Element Method (CVFEM) has been used [5].

A review of the literature exhibits that the unstructured mesh control volume methods have been developed to study the physics of coupled transfer (heat and mass) in porous media.

The intensification of transport in porous media has attracted many researches. Considerable researches have been developed more and more efficient methods (acoustic [6] and ultrasonic [7]). Recently, the employment of vibration technology in porous media has been an interesting subject and it has been found to enhance the coupled heat and mass transfer [8, 9].

At the last years, various research indicates the modelling of heat and mass transfer inside a porous exchanger. In those references, Sun et al. have explained the theoretical and the experimental study on heat and mass transfer of a porous ceramic tube [10]. Also, Chien et al. [11] have studied the heat and mass transfer of evaporative cooler with elliptic tube heat exchangers. An experimental and numerical study on heat and mass transfer characteristics in direct-contact total heat exchanger for flue gas heat recovery had developed by Wei et al. [12].

More and more recently, Yang et al. have studied the coupling effect of heat transfer in plate heat exchanger filled with porous media [13]. Also, Pourrahmani and Van Herle have developed an evaluation criterion of proton exchange membrane (ECPEM) fuel cells considering inserted porous media inside the gas flow channel [14]. An insight into CO2-CH4 hydrate exchange in porous media using magnetic resonance has presented by Li et al. [15]. Also, a solid–liquid model based on lattice Boltzmann method for phase change material melting with porous media in cylindrical heat exchangers is explained by Chen et al. [16]. Recently, such et al. have studied an enhancement of 3D mass and heat transfer within porous ceramic exchanger by Flow-induced vibration [17].

The aim of the present paper is to develop a numerical code that can explain the heat and mass transfer that arise inside a ceramic double partition brick. Moreover, we put the evolutions of parameters (temperature, liquid saturation, pressure) for coupled heat and mass transport during brick drying process. Also, a three-dimensional numerical code is employed to describe the transfer phenomena that arise during drying: temperature (T), saturation (S), pressure (P).

Several numerical results prove the efficiency of our code to study the coupled transfer of heat and mass during the drying of a complex geometry (double partition brick).

Numerical Study

The present problem is a numerical study of heat and mass transfer during double partition brick drying (porous medium). The geometry of the brick is a complex geometry defined by following figure:

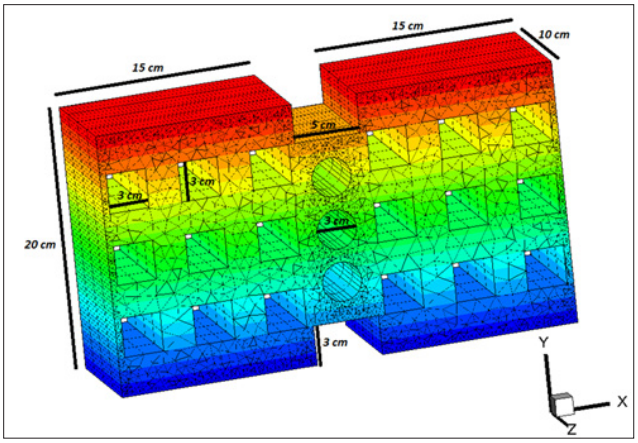

Figure 1: Double partition brick dimensions.

Equations System

The equations system is defined by Whitaker's theory [2]. A numerical system of heat and mass transfer is established for unsaturated porous media with the following assumptions:

- The porous medium is homogenous and isotropic and the three phases (solid, liquid and gas) are in local thermodynamic equilibrium.
- We negligee the radiative heat transfer, the viscous dissipation and the compression-work.
- The gaseous phase is ideal and the tortuosity and dispersion terms are used as diffusion term.

The macroscopic equations of heat and mass transfer in porous media are:

Generalized Darcy's Law

With Darcy's law, the average velocities (liquid phase $(\overline{V_l})$ and gaseous phase $(\overline{V_g})$) are:

Liquid Phase

$$\overline{V_l} = -\frac{KK_l}{\mu_l}\left[\nabla\left(\overline{P_g}^{g} - P_c\right) - \overline{\rho_l}^{l} g\right] \quad (1)$$

with $P_c = \overline{P_g}^{g} - \overline{P_l}^{l}$ presents the capillary pressure.

$$\overline{V_g} = -\frac{KK_g}{\mu_g}\nabla\overline{P_g}^{g} \quad (2)$$

Mass Conservation Equation

Liquid Phase

The equation of mass conservation for liquid phase is (liquid density is constant):

$$\frac{\partial \varepsilon_l}{\partial t} + \nabla(\overline{V_l}) = -\frac{\dot{m}}{\overline{\rho_l}} \quad (3)$$

And $\dot{m}$ is the rate mass of the evaporation.
ε_l is the fraction volume of liquid.

Gaseous Phase

The equation of mass conservation is:

$$\frac{d\overline{\rho_g}}{dt} + \nabla\left(\overline{\rho_g}^{g}\overline{V_g}\right) = \dot{m}_g \quad (4)$$

And $\overline{\rho_g}^{g}$ is the average density intrinsic of gaseous phase (this phase is considered as an ideal mixture of perfect gases).

Vapor Phase

$$\frac{d\overline{\rho_v}}{dt} + \nabla\left(\overline{\rho_v}^{g}\overline{V_v}\right) = \dot{m}_v \quad (5)$$

$$\overline{\rho_v}^{g}\overline{V_v} = \overline{\rho_v}^{g}\overline{V_g} - \overline{\rho_g}^{g} D_{eff}\nabla\left(\frac{\overline{\rho_v}}{\overline{\rho_g}^{g}}\right) \quad (6)$$

And D_{eff} presents the effective diffusion coefficient of vapor in porous medium. Also, this coefficient takes into account the resistance to the diffusion due to the constriction and the tortuosity effects.

Energy Conservation Equation

The energy conservation equation is defined as bellow:

$$\frac{\partial}{\partial t}\left(\overline{\rho C_p}\overline{T}\right) + div\left[\left(\overline{\rho_l}^{l} C_{Pl}\overline{V_l} + \sum_{k=a,V}\overline{\rho_k}^{g} C_{Pk}\overline{V_k}\right)\overline{T}\right] = \quad (7)$$

$$\nabla\left(\lambda_{eff}.\nabla\overline{T}\right) - \Delta H_{vap}\,\dot{m}_v$$

With ΔH_{vap} is the heat latent of vaporization at temperature T (K).
And λ_{eff} is the thermal effective conductivity of porous medium.

Also $\overline{\rho C_p}$ is the heat capacity of the porous medium defined as bellow:

$$\overline{\rho C_p} = \overline{\rho}_s C_{ps} + \overline{\rho}_l C_{pl} + \overline{\rho}_a C_{pa} + \overline{\rho}_v C_{pv} \quad (8)$$

Which $\overline{n}_s C_{ps}$, $\overline{n}_l C_{pl}$, $\overline{n}_v C_{pv}$ and $\overline{n}_a C_{pa}$ presents the mass heat capacities of three phases: solid, liquid and gas.

Thermodynamic Relations

The vapor pressure (partial pressure) is defined as bellow:

$$P_v = P_{veq}(T,S)$$

With S is the liquid saturation explained by:

$$S = \frac{\varepsilon_l}{\varepsilon} \quad (9)$$

For the gaseous phase, the pressure is defined by:

$$\bar{P}_i = \frac{\bar{\tilde{n}}_i}{M_i} R\bar{T} \;; i=a,v \quad (10)$$

$$\bar{P}g = \bar{P}a + \bar{P}v \quad \bar{\tilde{n}}_g = \bar{\tilde{n}}_a + \bar{\tilde{n}}_v$$

For the vapor phase, the pressure is:

$$\frac{Pv}{Pvs} = \exp\left(-\frac{2.\sigma.M_v}{r.\rho_l.R.T}\right) \quad (11)$$

Boundary Conditions

For our equations system, the boundary conditions are defined as bellow: the temperature, saturation and pressure are uniform inside the brick (Figure 2).

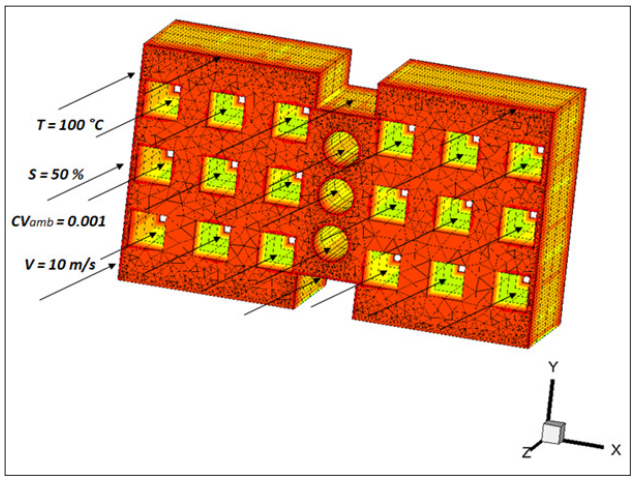

Figure 2: Boundary conditions.

The boundary conditions for our model are:

The exchanging faces: right, left and up faces and cavities:

$$\left[\lambda_{eff}\frac{\partial\langle T\rangle}{\partial X_i} + \Delta H_{vap}\rho_l\langle V_l\rangle n_i\right] = h_t\left(\langle T\rangle - T_\infty\right) \quad (12)$$

The mass flow (evaporation and evacuation):

$$\left[\rho_l\langle V_l\rangle + \langle \rho_v\rangle^g\langle V_v\rangle\right]n_i = h_m\left(C_{vs} - C_{v\infty}\right) \quad (13)$$

On exchanging faces, the pressure is considered as the atmospheric pressure:

$$\left[\langle P_g\rangle^g\right] = P_{atm} \quad (14)$$

The bottom face is considered as adiabatic and impermeable face.

$$\left[\lambda_{eff}\frac{\partial\langle T\rangle}{\partial X_i} + \Delta H_{vap}\rho_l\langle V_l\rangle n_i\right] = 0 \quad (15)$$

$$\left[\rho_l\langle V_l\rangle + \langle \rho_v\rangle^g\langle V_v\rangle\right]n_i = 0 \quad (16)$$

$$\left[\frac{\partial\langle P_g\rangle^g}{\partial X_i}\right] = 0 \quad (17)$$

The convective coefficients (heat and mass transfer) are explained in Table 1.

	Cavities [18]	Faces [19]
h_t	$\frac{\lambda \times 0.023 \times Re^{4/5} \times Pr^{1/3}}{D}$	$\frac{\lambda \times 0.023 \times Re^{4/5} \times Pr^{1/3}}{L_C}$
h_m	$\frac{D_{A,B} \times 0.023 \times Re^{4/5} \times Sc^{1/3}}{D}$	$\frac{D_{A,B} \times 0.023 \times Re^{4/5} \times Sc^{1/3}}{L_C}$
Validity conditions	$10^4 < Re < 1.2 \times 10^5$ $0.6 \le Pr \le 160$ $0.6 \le Sc \le 160$	$Re < 5 \times 10^5$ $Pr \ge 0.6$ $Sc \ge 0.6$
Re	$\frac{\rho_a w_a D}{\mu_a}$	$\frac{\rho_a w_a L_C}{\mu_a}$
	$Pr = \frac{C_a \mu_a}{\lambda_a}$	$Sc = \frac{\vartheta_a}{D_{A,B}}$

Table 1: Heat and mass transfer coefficients.

With:

h_t : is the convective coefficient of heat transfer [W/(m² °C)]

h_m: is the convective coefficient of mass transfer [m/s]

$D_{A,B}$: presents the vapor diffusion in air defined as bellow:

$D_{A,B} = D_{vap,air} = 0.26 \times 10^{-4}$ [m²/s]

$L_C = 0.1$ m : is the characteristic length of the exchanger.

Numerical Solution

The Control Volume Finite Element Method (CVFEM) is used to solve our system of equations [20, 21]. Moreover, the control volume is composed of triangular elements which implies the grid flexibility. Also, this numerical method ensures the conservation of flux.

To describe the mesh generation, we use the free mesh generator Gmsh [22] (Figure 3).

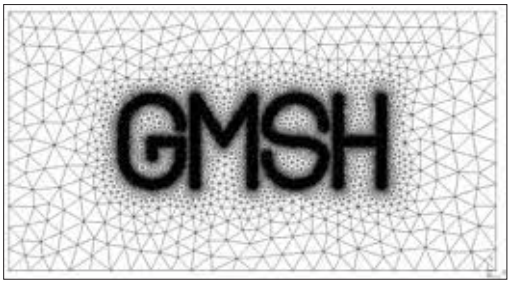

Figure 3: Gmsh.

For our simulation, we develop a numerical code (FORTRAN) and to validate our results, our model is validated by a convective heat and mass transfer experiment developed by Saber Chemkhi [23].

The conditions of validation are listed in Table 2.

T_{amb} (°C)	40	50
T_{ini} (°C)	25	
Initial water content (kg/kg b. s)	0.1995	
C_{Vamb}	0.01	
P_{amb} (atm)	1	
Relative humidity (%)	40	
Air velocity (m/s)	2	

Table 2: Validation conditions.

In Figure 4, we present the validation of our code with the evolution of water content.

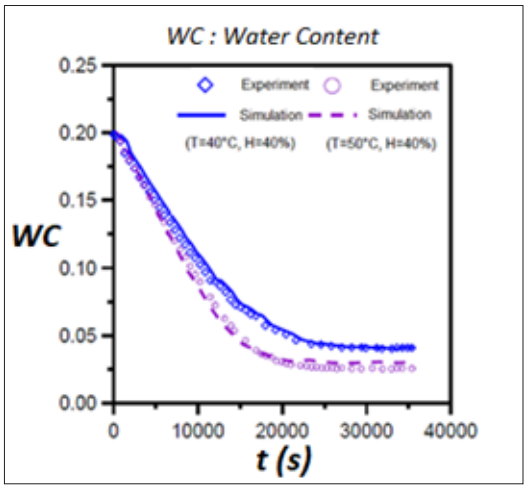

Figure 4: Validation code (water content).

However, we can say that there is a great agreement between our numerical simulation and the experimental results.

Results and Discussions

In this section, we present the numerical results obtained from the compilation of our code which is applied to the heat and mass transfer during double partition brick drying.

This numerical study is composed of temperature, saturation, pressure and water content evolutions.

To simulate the 3D heat and mass transfer phenomenon that arise during drying process, we use the free mesh generator Gmsh. (Figure 5).

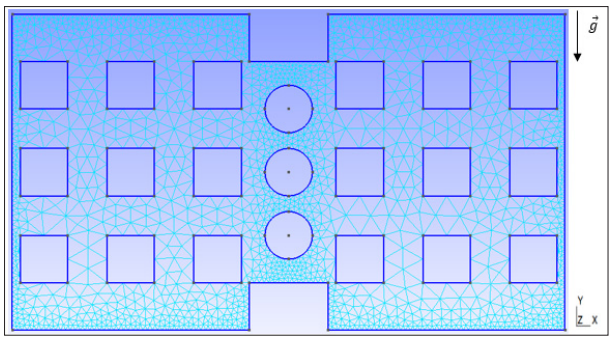

Figure 5: Brick meshing.

The numerical parameters used in this code are presented in Table 3.

T(°C)	S(%)	V(m/s)	P_o (%)	CV_{amb}	P_{amb}(atm)
100	50	10	30	0,0001	1

Table 3: Numerical code parameters.

The simulation results are established for three nodes aligned on the z axis:

- Z = 0
- Z = Lc/4
- Z = Lc/2

Temperature Evolution

In this part, we present the time evolution of temperature (Figure 6).

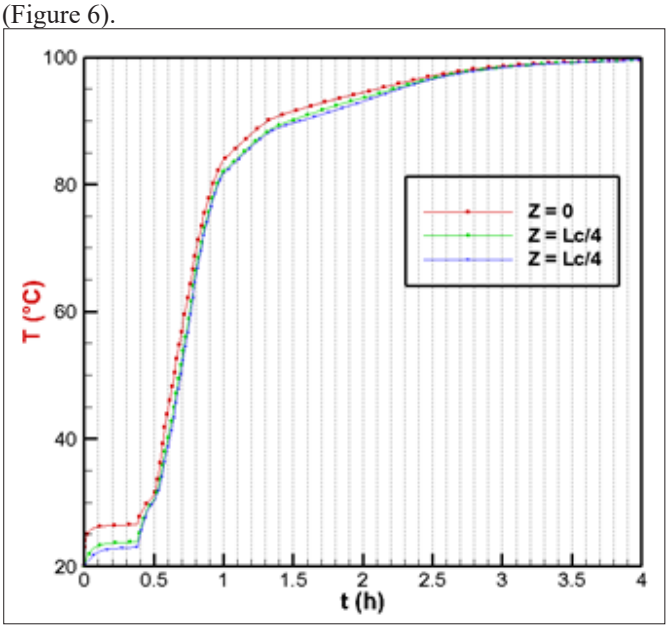

Figure 6: Temperature evolution.

Referring to Figure 6, we can note that the evolution of temperature is more rapid for the node closest to the exchange surface (Z = 0 > Z = Lc/4 > Z = Lc/2) which promotes the heat exchange during the drying process.

Saturation Evolution

In this part, we present the time evolution of saturation during drying process (Figure 7).

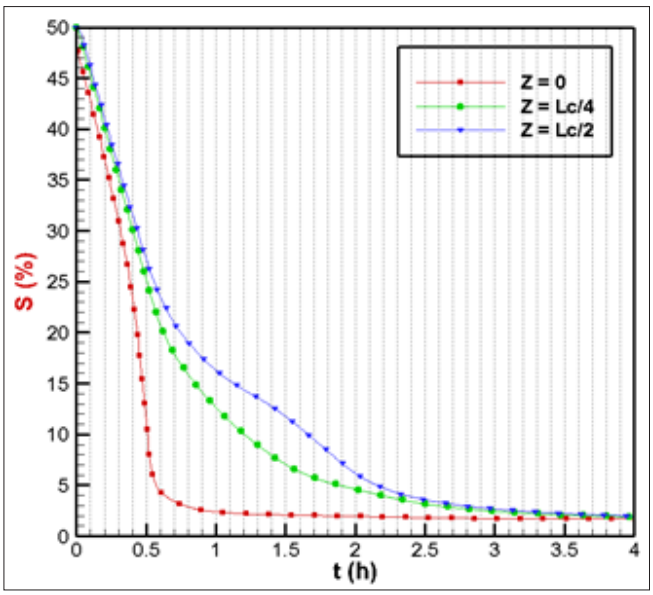

Figure 7: Saturation evolution.

Figure 7 presents a comparison of the evolution of liquid saturation for three nodes placed on the brick. This figure shows a decrease over time and this decrease is slower for the nodes inside the brick.

Pressure Evolution

For this part, we depict the pressure evolution in time (Figure 8).

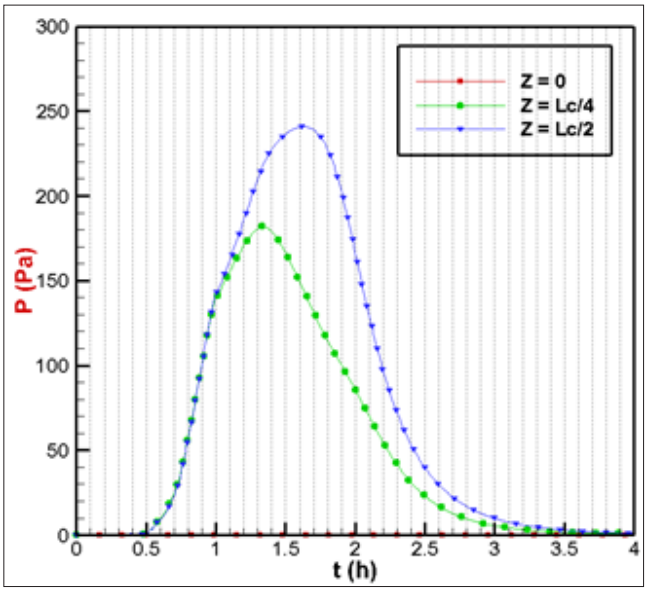

Figure 8: Pressure evolution.

Based in Figure 8, we can conclude that the great peak of pressure is linked to the node inside the brick with a large amount of water.

Water Content Evolution

Also, we have studied the time evolution of water content during the drying process (Figure 9).

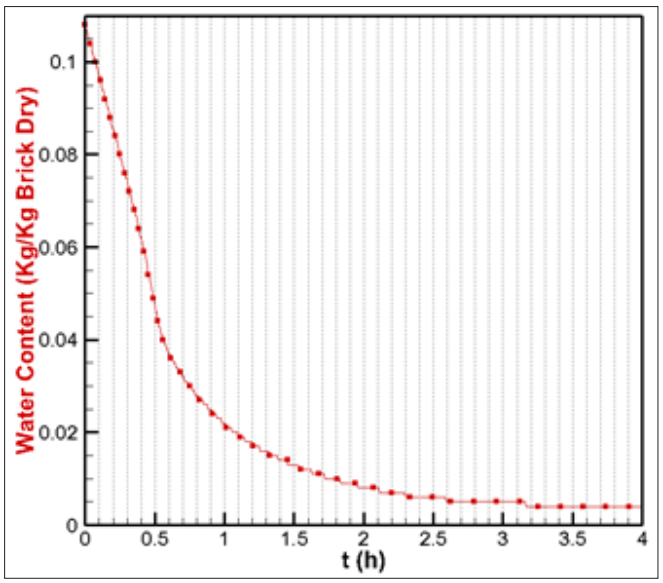

Figure 9: Water content evolution.

In Figure 9, we observe that water content decreases over time and it approaches to the zero value.

Our numerical model verifies the four classic drying phases:

- **Preheating period:** During this first period, the mass and heat fluxes are initiated. The heat transfer is related to the supply of energy from the drying air to the porous material to evaporate water on the surface.
- **Period at constant speed:** This phase is characterized by a thermal equilibrium and the transport of free water in the material is fast enough to feed the surface which is the place of evaporation. The porous material remains saturated with water in the case of highly deformable media. This involves a contraction of the solid structure to fill the voids left by the evaporated water: This is the volume shrinkage of the material.
- **First slowing period:** The beginning of this period corresponds to the entry of the surface of the porous material into the hygroscopic field. Then, a drying front is created corresponding to the place of evaporation of the water which separates the medium into two zones (saturated and unsaturated).
- **Second slowing period:** The drying rate decreases sharply when all the free water has been evaporated. The removal of bound water requires an additional energy input: This energy is the binding energy of adsorbed water.

To better understand the mechanisms that arise during heat and mass transfer during porous brick drying, we have shown:

- The spatiotemporal evolutions of temperature, saturation and pressure for three time of drying (Figures 10-12): Beginning (**5 Min**); Middle (**40 min**); End (**2 h**).
- The slice's view to represent the distribution of three parameters (T; S; P) (Figures 13-15).

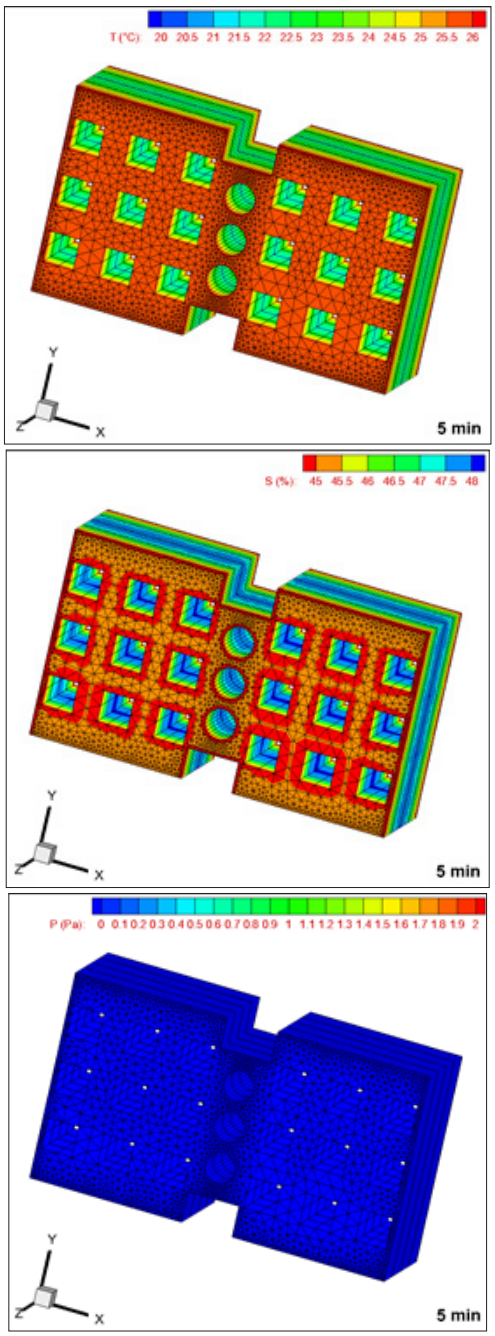

Figure 10: Three-dimensional distribution of temperature, saturation and pressure at the beginning of drying.

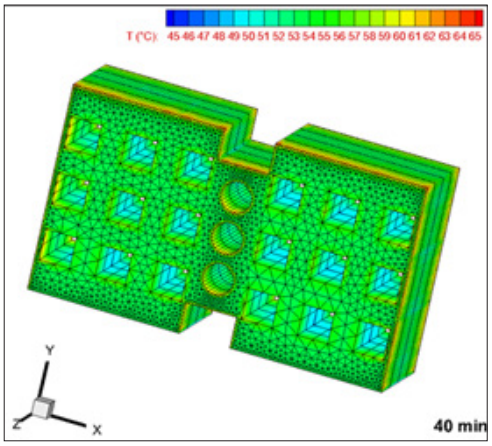

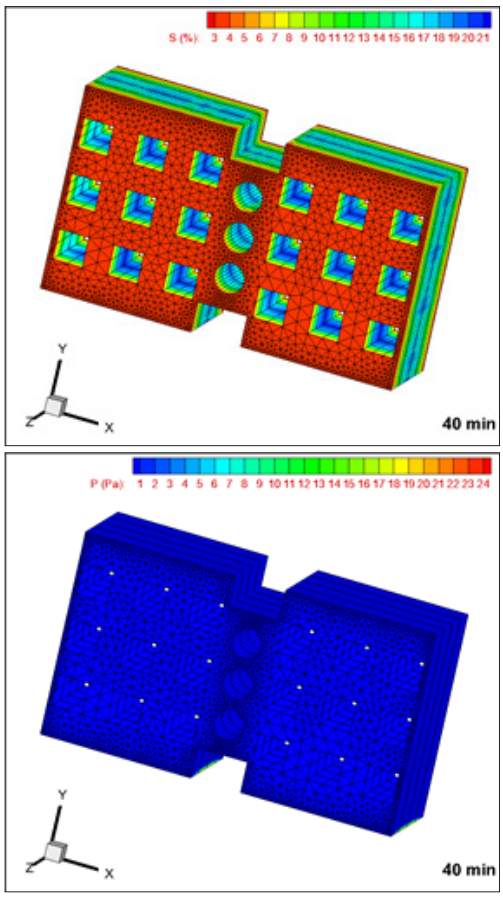

Figure 11: Three-dimensional distribution of temperature, saturation and pressure at the middle of drying.

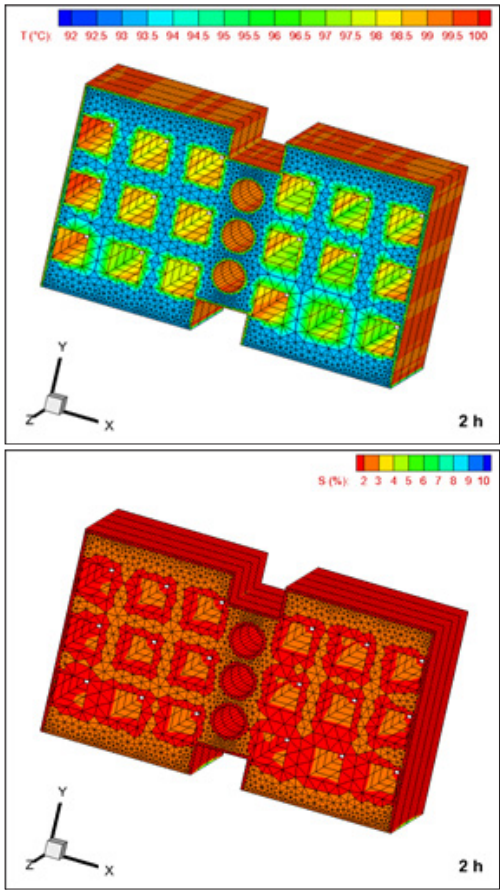

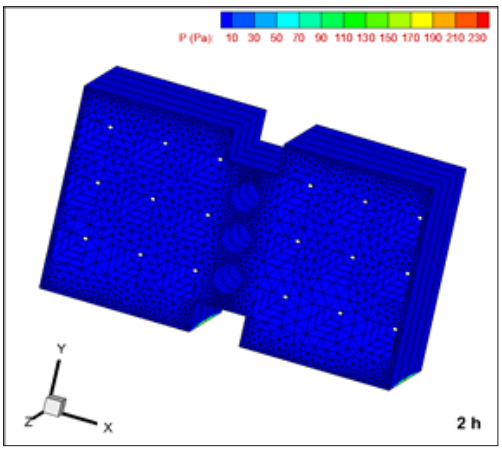

Figure 12: Three-dimensional distribution of temperature, saturation and pressure at the end of drying.

Referring to those results (Figures 10-12), we can note that:

- The heat and mass exchange is more intense for the cavities and the exchange faces and less rapid inside the brick (the temperature gradient had place to supply the energy necessary for the evaporation).
- The exchange faces force the evaporation of liquid.
- The lower side is characterized by a slow and less intense drying given the amount of water that accumulates on this side.

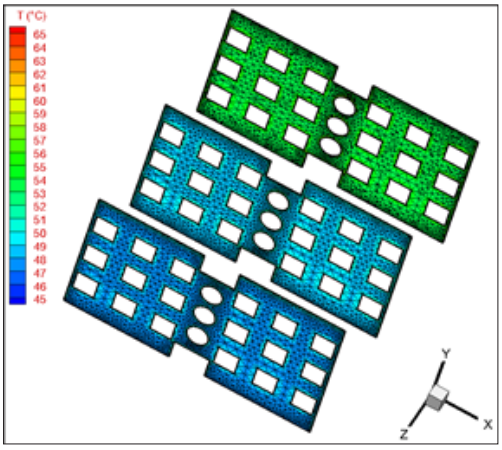

Figure 13: Slice's view distribution of temperature.

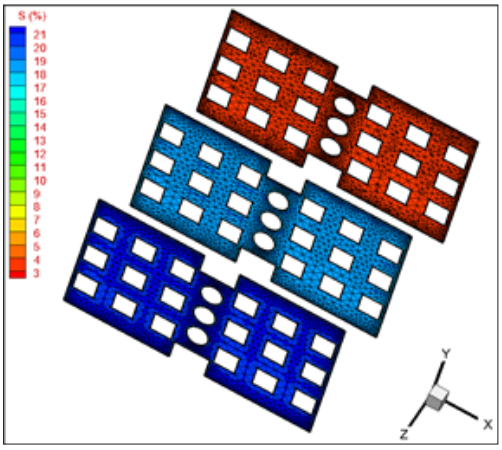

Figure 14: Slice's view distribution of liquid saturation.

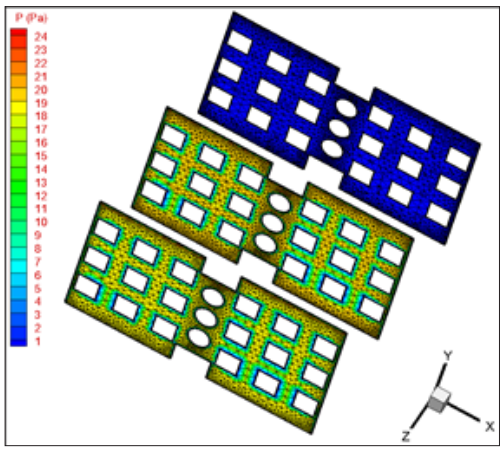

Figure 15: Slice's view distribution of gaseous pressure.

Based in Figures 13-15, we can note that the exchange faces (faces and cavities) are characterized by a faster and more intense drying process. Moreover, the temperature profile is more important for these faces and the amount of liquid is greater inside the brick. Also, the pressure distribution is more intense in the vicinity of the middle and in the bottom of double partition brick.

Conclusion

In the present study, a 3-D numerical model is established to analyze the coupled heat and mass transfer that arise during double partition brick drying process. This numerical code highlights the understanding of phenomena occurring within the porous drying. The mesh is generated by the free mesh generator Gmsh and a numerical code has been developed for three-dimensional simulation of the convective transfer of porous brick drying.

The numerical code simulates the evolution of temperature, liquid saturation and gaseous pressure during the drying process. Moreover, the present model explains the coupled heat and mass transport that arise inside a complex geometry. Also, the drying is well established after 4 hours and the physical analysis in this paper proves the importance and the originality of this code.

Nomenclature

C_a	specific heat of the air $[kJ/kgK]$
C_p	specific heat at constant pressure $[kJ/kgK]$
C_v	specific heat of the vapor $[kJ/kgK]$
C_w	specific heat of the water $[kJ/kgK]$
$D_{A,B}$	diffusion coefficient [m²/s]
g	gravitational acceleration [m/s²]
h_m	convective mass transfer coefficient$[m/s]$
h_t	convective heat transfer coefficient$[W/m2^oC]$
K	intrinsic permeability $[m^2]$
L_c	characteristic length of brick $[m]$
M_a	molar mass of air [kg/mol]
Mv	molar mass of vapour [kg/mol]
m	evaporation rate [kg/s]
n_i	outward normal vector
P	pressure [Pa]

Pc capillary pressure [Pa]
Po Exchanger porosity [%]
P_{Vs} partial pressure of saturated vapour [Pa]
R gas constant [kJ/(kmol K)]
r characteristic magnitude that represents the average radius of curvature of the menisci if the retention forces of the liquid are of capillary origin
S liquid saturation [%]
T temperature [K]
t time [s]
wa air velocity [*m/s*]

Greek Symbols

ε porosity
ε_l volume fraction of liquid phase
μ dynamic viscosity [kg/ms]
ϑ kinematic viscosity [m^2/s]
ρ density [kg/m^3]
λ conductive transfer coefficient [W/m^oC]
σ surface tension [*N/m*]
ΔH_{vap} vaporisation latent heat [J / Kg]

Subscripts

0 initial condition
a air
eff effective
g gas
l liquid
v vapor
vs vapor saturated

Dimensionless groups

Re Reynolds number
Pr Prandtl number
Sc Schmidt number

Appendix

Characteristics of double partition brick and air used are:

Double partition brick:

Material properties	Values used for the computations
Porosity	0,36
Density of solid matrix	$\rho_s = 2.6 \times 10^3$ (kg m^3)
Specific heat capacity of solid matrix	$C_{ps} = 8.79 \times 10^2$ (J kgK)
Specific heat capacity of liquid	$C_{pl} = 4.22 \times 10^3$ (J kgK)
Specific heat capacity of vapor	$C_{pv} = 1.86 \times 10^3$ (J kgK)
Liquid dynamic viscosity	$\mu_l = 6.5 \times 10^{-4}$ (kg ms)
Vapor dynamic viscosity	$\mu_v = 1.860 \times 10^{-5}$ (kg ms)
Intrinsic liquid permeability	2.5×10^{-14} (m^2)
Relative liquid permeability	$K_l = X^{*3}$ with $X^* = \frac{X - X_{ir}}{X_{sat} - X_{ir}}$ and $X_{ir} = 0.3$
Relative gaseous permeability	$K_{rg} = 1 + (2X^* - 3)X^{*2}$
Capillary pressure	$P_c = \frac{\varepsilon}{K}^{\frac{1}{2}} \sigma J(s)$ with $J(s) = 0.364\ 1 - \exp(-40(1 - s)) + 0.221(1 - s) + \frac{0.005}{s - 0.05}$ and $\sigma(T) = (121.2 - 0.167T)10^{-3}$
Vapor pressure	$< ?_v > = < P_{vs} > [- \frac{2\sigma M_v}{r\rho_l R < ? >}]$ With $\log_{10} r = 2.16 \times 10^{-2} + 43.85 - 253.5 \times S^2 - 794.54 \times S^3 - 1333.7 \times S^4 + 1111 \times S^5 - 352.5 \times$
Thermal conductivity	$\lambda_{eff} = (\lambda_g^a \varepsilon - \varepsilon_l + \lambda_l^a \varepsilon_l + \lambda_s^a (1 - \varepsilon))^{1/a}$ (W mK With $a = 0.25$

Air

Material properties	Values used for the computations
Specific heat capacity	$1006\ (J/kgK)$
Thermal conductivity	$0.026\ (W/mK)$
Density	$1.17\ (kg/m^3)$
Dynamic viscosity	$1.15 \times 10^{-5}\ (kg/ms)$

References

1. A.V. Luikov, (1975). Systems of differential equations of heat and mass transfer in capillary porous bodies (review), *Int. J. Heat Mass Transfer*, Vol. 18, pp. 1–14.
2. S. Whitaker, (1977)."Simulation heat, mass and momentum transfer in porous media a theory of drying", Advances in Heat Transfer, Vol. 13, pp. 119-203. Academic Press. New York.
3. A.E. Kabeel, M. Abdelgaied, (2016). Numerical and experimental investigation of a novel configuration of indirect evaporative cooler with internal baffles, Energy Convers. Manage. 126, 526–536.
4. H.D. Hettiarachchi, M. Golubovic, W.M. Worek, (2007). The effect of longitudinal heat conduction in cross flow indirect evaporative air coolers, Appl. Therm. Eng. 27 (11), 1841–1848.
5. Fung, L. S., Hiebert, A. D., Nghiem, L. (1991). Reservoir simulation with a control volume finite element method, SPE 21224. 11th SPE Symp. on Reservoir Simulation, Anaheim, February 17–20.
6. S.J. Kowalski, (2015). Ultrasound in wet materials subjected to drying: A modelling study, International Journal of Heat and Mass Transfer. 84, 998-1007.
7. V. Acosta, J. Bon, E. Riera, A. Pinto, (2015). Ultrasonic drying processing chamber, Physics Procedia. 70, 854-857.
8. R. Rzig, N. Ben Khedher, S. Ben Nasrallah, (2017). A 3-D numerical heat and mass transfer model for simulating the vibration effects on drying process, Heat Trans. Asian Res. 46, 1204-1221.
9. N. Ben Khedher, R. Rzig, I.A. Alatawi. (2020). Numerical comparison of triangular and sinusoidal external vibration effects on 3D porous drying process. *Engineering, Technology & Applied Science Research. 10* (2), 5554-5560.
10. Sun, T., Huanga, X., Qua, Y., Wangb, F., Chen, Y. (2020). Theoretical and experimental study on heat and mass transfer of a porous ceramic tube type indirect evaporative cooler. Applied Thermal Engineering, 173, 115-211.
11. Chien, L.H., Chen, D.C., Liu, Y.J., Yan, W.M., Ghalambaz, (2021). M. Heat and mass transfer of evaporative cooler with elliptic tube heat exchangers- an experimental study. International Communications in Heat and Mass Transfer. 127, 105-502.
12. Wei, H., Huang, S., Zhang, X. (2022). Experimental and simulation study on heat and mass transfer characteristics in direct-contact total heat exchanger for flue gas heat recovery. Applied Thermal Engineering 200, 117-657.
13. K. Yang, X. Li, K. Liu, J. Wang. (2022). Coupling effect of heat transfer in plate heat exchanger filled with porous media. International Journal of Heat and Mass Transfer. Vol. 182.
14. H. Pourrahmani, J. Van Herle. (2022). Evaluation Criterion of Proton Exchange Membrane (ECPEM) fuel cells considering inserted porous media inside the gas flow channel. Applied Thermal Engineering. Vol. 203.
15. M. Li, A. Rojas Zuniga, P. L. Stanwix, Z. M. Aman, E. F. May, M. L. Johns. (2022). Insights into CO2-CH4 hydrate exchange in porous media using magnetic resonance. Fuel. Vol. 312.
16. D. Chen, A. Riaz, V. C. Aute, R. Radermacher (2022). A solid–liquid model based on lattice Boltzmann method for phase change material melting with porous media in cylindrical heat exchangers. Applied Thermal Engineering. Vol. 207.
17. R. Rzig, F. Troudi, N. Ben Khedher, I. Boukholda, F. A. Alshammari, N. Alshammari. (2022). Enhancement of 3D mass and heat transfer within porous ceramic exchanger by Flow-induced vibration. ACS Omega.
18. F.W. Dittus, L.M.K. (1985). Boelter, Heat transfer in automobile radiators of the tubular type, reprinted in: Int. Comm. Heat Mass Transfer, 12; 3–22.
19. F.P. Incropera, D.P. De Witt, Fundamentals of Heat and Mass Transfer, John Wiley & Sons, New York, USA, 2002.
20. Balliga BR, Patankar SV., (1980). A new finite-element formulation for convection–diffusion problems, Numer Heat Transfer, 3, 393–409.
21. Balliga BR, Patankar SV, (1983). A control-volume finite element method for two-dimensional fluid flow and heat transfer, Numerical Heat Transfer, 6, 245–6.
22. Christophe Geuzaine, Jean-François Remacle, (2009). Gmsh: A 3-D finite element mesh generator with built-in pre- and post-processing facilities, International Journal for Numerical Methods in Engineering, 79 (11), 1309–1331, 10.
23. S. Chemkhi, (2008). Thesis Drying of an unsaturated deformable middle: modeling of hygro-mechanical coupling, doctoral dissertation, Bordeaux 1 University.